

Ehsan Kazemi and Stefan Heinz*

Dynamic Large Eddy Simulations of the Ekman Layer Based on Stochastic Analysis

DOI 10.1515/ijnsns-2015-0049

Received April 19, 2015; accepted December 29, 2015

Abstract: Large eddy simulation (LES) of the neutrally stratified turbulent Ekman layer is performed. In particular, we compare three LES models with direct numerical simulation (DNS), which was validated against existing DNS. The models considered are a standard nondynamic LES model, the Smagorinsky model (SM), a standard dynamic LES model, the stabilized dynamic Smagorinsky model (DSM), and a new linear dynamic model (LDM), which was derived from a realizable stochastic turbulence model. The following conclusions are obtained. The SM does not represent an appropriate model for the flow considered. Mean velocity and turbulence intensities are poorly predicted. With respect to instantaneous fields, the SM provides a tilting of turbulence structures in the opposite direction as seen in DNS. The stabilized DSM also suffers from significant shortcomings. First, its behavior depends on the wall distance. Close to the wall, it produces acceptable turbulence structures. Away from the wall, it suffers from the same shortcomings as the SM. Second, it incorrectly describes the effect of grid coarsening. The new LDM is free from the disadvantages of the SM and stabilized DSM. Its predictions of both mean and instantaneous velocity fields agree very well with DNS. The relevant conclusion is the following. The use of a dynamic LES method represents a mean for correctly simulating large-scale structures (means and stresses), but it does not ensure a correct simultaneous simulation of small-scale structures. Our results indicate that a dynamic method designed in consistency with a realizable stress model can correctly simulate both large-scale and small-scale structures.

Keywords: large eddy simulation, dynamic subgrid-scale modeling, Ekman layer

PACS® (2010). 47.27.E-, 47.27.ep, 47.32.Ef

*Corresponding author: **Stefan Heinz**, Department of Mathematics, University of Wyoming, 1000 East University Avenue, Laramie, WY 82071, USA, E-mail: heinz@uwyo.edu

Ehsan Kazemi, Department of Mathematics, University of Wyoming, 1000 East University Avenue, Laramie, WY 82071, USA

1 Introduction

The wide spectrum of multiscale motions involved in turbulent flows can be fully resolved by using direct numerical simulation (DNS). However, in practice DNS is only applicable to low Reynolds number flows, this means flows exhibiting a relatively small spectrum of scales, because the computational cost of DNS are way too high to perform high Reynolds number turbulent flow simulations. The use of Reynolds-averaged Navier–Stokes equations (RANS) represents a computationally cheap alternative to DNS, but RANS cannot resolve any of the multiscale turbulent motions. Therefore, the use of large eddy simulation (LES) represents the most promising way to simulate multiscale turbulent flows, this means flows at moderate Reynolds numbers [1–8].

However, many relevant turbulent flow simulations involve the need to account for walls. Walls change significantly the structure of turbulent flows, in particular via damping effects on the turbulence. LES of wall bounded flows significantly suffer from the problem to reflect such wall damping effects. The explicit modeling of wall damping effects via damping functions is the concern of research over many decades [7]. The use of dynamic LES methods that are capable of using optimal local and instantaneous model parameters represents a very promising approach [9–13], but the existence of a large variety of such dynamic LES methods also reveals questions related to the use of such methods. The need to account for additional effects like rotation can add a lot of complexity to these problems.

Given the variety of dynamic and nondynamic LES methods that are currently in use, it is a valid goal to develop methods that are based on sound physics. Such LES methods can be obtained on the basis of stochastic analysis of turbulence [2–5, 14–16]. In contrast to many other methods, LES based on stochastic analysis honors the realizability principle (see Section 2.4), which was found to be a fruitful concept for the design of turbulence models. Nevertheless, only a preliminary analysis of basic features of such realizable dynamic LES models was presented so far on the basis of channel flow simulations at one relatively low Reynolds number [16].

The goal of this paper is to analyze the performance of the recently suggested new realizable dynamic LES model [15, 16] with respect to a turbulent flow affected by rotation. In particular, we consider the Ekman layer, which is often considered as a simple model of the atmospheric boundary layer (ABL) [17–25]. This flow is significantly more complex than a simple channel flow, the only flow considered so far. The involvement of rotation implies a very different and varying structure of turbulent stresses than seen in channel flows. It may be expected that wall damping function concepts used to correct the turbulent shear stress in channel flows are inapplicable to flows that are significantly affected by rotation. The question is how dynamic LES methods, which do not include explicit wall damping functions, are capable of dealing with this problem.

More specifically, we consider the neutrally stratified Ekman layer at one relatively low Reynolds number. Recent analysis of realizable dynamic LES models showed that the consideration of instantaneous velocity fields represents a very fruitful tool to get a much better insight into the nature and differences of dynamic and nondynamic LES methods [16]. To enable such analysis of instantaneous turbulence structures we had to perform DNS for comparisons, and such DNS was only affordable at a relatively low Reynolds number. To show the differences between the realizable dynamic LES model considered and conventional LES methods we used two standard LES methods for comparisons: a nondynamic LES model that applies a damping function, and the stabilized dynamic Smagorinsky model (DSM).

The paper is organized in the following way. Section 2 introduces the LES methods considered. The computational methods applied to solve these equations are presented in Section 3. The basic problem related to the use of dynamic LES methods is the development of methods that are computationally stable. To address related questions, we analyze stability features of the models considered in Section 4. The model performance with respect to turbulence simulations will be analyzed in Section 5. Section 6 deals with conclusions of this analysis.

2 Modeling approaches

The LES modeling approaches applied below are based on the incompressible Navier–Stokes equations for filtered velocities \tilde{u}_i ($i=1, 3$),

$$\frac{\partial \tilde{u}_i}{\partial x_i} = 0, \quad (1)$$

$$\frac{\tilde{D}\tilde{u}_i}{\tilde{D}t} = -\frac{1}{\rho} \frac{\partial P}{\partial x_i} + 2\nu \frac{\partial \tilde{S}_{ij}}{\partial x_j} - \frac{\partial \tau_{ij}^d}{\partial x_j} - 2\varepsilon_{3ji} \tilde{\Omega}_j \tilde{u}_i. \quad (2)$$

Here, $\tilde{D}/\tilde{D}t = \partial/\partial t + \tilde{u}_k \partial/\partial x_k$ denotes the filtered Lagrangian time derivative, ρ is the constant mass density, $P = \tilde{p} + 2k/3$ is the modified filtered pressure that includes a contribution due to the subgrid-scale (SGS) kinetic energy $k = \tau_{ii}/2$. $\tilde{S}_{ij} = (\partial \tilde{u}_i/\partial x_j + \partial \tilde{u}_j/\partial x_i)/2$ is the filtered rate-of-strain tensor, ν is the constant kinematic viscosity and τ_{ij}^d refers to the deviatoric part of SGS stress tensor τ_{ij} . The summation convention is used for repeated indices. The last term on the right-hand side of eq. (2) reflects the Coriolis force effect. The wall normal direction is x_3 (z), the corresponding velocity component is u_3 (w). $\tilde{\Omega}_j$ refers to the rotation vector. The permutation symbol ε_{ijk} is $+1$ for cyclic values of ε_{ijk} , -1 for anticyclic values, and 0 if an index is repeated. The numerical grid with a filter width $\Delta = (\Delta_1 \Delta_2 \Delta_3)^{1/3}$ is used as LES filter.

Equation (2) is unclosed as long as the deviatoric SGS stress tensor τ_{ij}^d is not defined. We will apply the usual eddy-viscosity model for τ_{ij}^d ,

$$\tau_{ij}^d = -2\nu_t \tilde{S}_{ij} = -2C_s \Delta^2 |\tilde{S}| \tilde{S}_{ij}. \quad (3)$$

The SGS viscosity ν_t is defined via the last expression. Here, $|\tilde{S}| = (2\tilde{S}_{ij}\tilde{S}_{ji})^{1/2}$ refers to the characteristic rate-of-strain rate, and C_s is a model parameter. The three LES models described in the following subsections differ by their different ways to define the model parameter C_s .

2.1 The Smagorinsky model (SM)

The Smagorinsky model (SM) is often applied in LES because of its simplicity and computational stability. The SM applies a constant positive value for the model coefficient C_s . For example, Lilly [26] suggested the value of $C_s = 0.17^2$. However, there are two main problems associated with the use of a constant C_s . First, a constant C_s turned out to be inappropriate to accurately calculate, for example, laminar flows, transitional flows and near-wall regions. Second, the resulting model cannot account for backscatter of energy from the small scales to large scales, which requires negative C_s values.

According to observations made on the basis of DNS, a minimum requirement for the proper simulation of a wall-bounded turbulent flow as considered here is to reflect the need to decrease the value of C_s with decreasing distance from the wall. To do so, we use

the C_S damping model of De Villiers [27], which follows suggestions made by Mason and Thomson [28, 29],

$$C_S = \left[\min \left(C_0, \kappa z \left[1 - e^{-z^+ / A^+} \right] / \Delta \right) \right]^2. \quad (4)$$

Here, $z^+ = zu^* / \nu$ (see Section 3.1), $C_0 = 0.17$, $\kappa = 0.42$, and $A^+ = 26$. The combination of the SGS model (3) with eq. (4) for C_S will be referred to below as SM.

2.2 The dynamic Smagorinsky model (DSM)

Compared to the application of the SM, a dynamic method for calculating C_S offers many advantages. Such models are well applicable to laminar flows, transitional flows and wall-bounded flows such that the relevant backscatter of energy can be accounted for. The model considered here is the dynamic model suggested by Germano [9, 10] combined with Lilly's modification [12], which forms the basis for many dynamic LES models,

$$C_S = - \frac{L_{ij}^d H_{ij}}{H_{mn} H_{mn}}. \quad (5)$$

Here, H_{ij} and the Leonard stress tensor L_{ij} , which enters eq. (5) via its deviatoric part L_{ij}^d , are given by

$$H_{ij} = 2(\Delta^T)^2 \left| \bar{\bar{S}} \right| \bar{\bar{S}}_{ij} - 2(\Delta)^2 \left| \bar{S} \right| \bar{S}_{ij}, \quad L_{ij} = \overline{\bar{u}_i \bar{u}_j} - \bar{\bar{u}}_i \bar{\bar{u}}_j. \quad (6)$$

Here, the overbar refers to the test filter operation, and Δ^T is the test filter width. It is worth noting that both H_{ij} and L_{ij} are available in simulations. The combination of the SGS model (3) with eq. (5) for C_S will be referred to below as original DSM.

Unfortunately, the original DSM usually cannot be applied in simulations. It leads to the appearance of large negative values of C_S , which imply computational instabilities. To stabilize the DSM, we will apply eq. (5) averaged along cell faces,

$$C_S = - \frac{\langle L_{ij}^d H_{ij} \rangle}{\langle H_{mn} H_{mn} \rangle}, \quad (7)$$

where $\langle \dots \rangle$ refers to a local averaging over cell faces. The latter means that face values of dynamic coefficients were obtained by interpolation of cell values. Face-averaged dynamic coefficient values were calculated then as average of face values multiplied with their relative weight, which is the ratio of the face area considered to the total face area. Hence, the averaging applied is different from the averaging of adjacent cell values. In addition, the total viscosity $\nu + \nu_t$ is clipped to zero whenever it is negative. The combination of the SGS

model (3) with eq. (7) for C_S will be referred to below as stabilized DSM.

2.3 The realizable linear dynamic model (LDM)

As an alternative to the SM and stabilized DSM, we also consider another dynamic LES model [15, 16],

$$C_S = - \frac{L_{ij}^d M_{ji}}{M_{kl} M_{lk}}. \quad (8)$$

Here, L_{ij}^d is defined according to expressions (6), and the matrix M_{ij} is given by the expression

$$M_{ij} = 2(\Delta^T)^2 \left| \bar{\bar{S}} \right| \bar{\bar{S}}_{ij}. \quad (9)$$

The combination of the SGS model (3) with eq. (8) for C_S will be referred to below as realizable linear dynamic model (LDM). Comments about this model, which will be used here without any averaging or clipping of the dynamic coefficient, will be made in the following section.

2.4 Realizable versus nonrealizable dynamic models

The essential difference between eq. (8) and the two DSM models (5) and (7) is that they are based on different assumptions for the deviatoric Leonard stress L_{ij}^d . Both DSM models assume $L_{ij}^d = -C_S H_{ij}$, whereas the LDM applies $L_{ij}^d = -C_S M_{ij}$. The expressions for C_S are implied by the corresponding L_{ij}^d assumptions [15, 16]: by defining a quadratic error of L_{ij}^d assumptions (which is implied by any setting of C_S) and minimizing this error, one obtains eqs (8) and (5).

Recent analyses of channel flow data [16] demonstrated that the L_{ij}^d model assumption used by the LDM represents a much more appropriate concept than the corresponding model assumptions used by the two DSM models. This difference is caused by the fact that the DSM model assumption is a purely empirical concept, whereas the LDM model assumption is derived from a stochastic turbulence model that honors the realizability requirement [15, 16]. The realizability requirement enunciates the rudimentary expectation that an acceptable turbulence closure model be based on the statistics of a velocity field that is physically achievable or realizable. It is recognized as an important guiding principle for turbulence modeling [1, 7, 30–33]. It is worth noting that the

LDM stress model derived from a stochastic turbulence model does not only satisfy the realizability requirement in the sense that it is implied by a realizable stochastic turbulence model. It also satisfies the realizability requirement in the Schumann sense [32], which means the LDM provides a SGS stress that is positive semi-definite. The latter fact was shown by the simulations reported below on several (A1, A2, A3, and other) grids by asking whether Schumann's realizability conditions $\tau_{ii} \geq 0$, $|\tau_{ij}| \leq (\tau_{ii}\tau_{jj})^{1/2}$, and $\det(\tau_{ij}) \geq 0$ are satisfied. This was done by approximating the turbulent kinetic energy k by an local equilibrium expression [15]. It was found that the realizability conditions were only violated in less than 0.5% of grid points. Such minor violations can be attributed to the k approximation applied.

3 Computational methods

The computational methods applied will be described next. This will be done with respect to the simulation setup, the numerical realization of DNS and LES, and the validation of DNS in the following three subsections, respectively. The validation of LES versus DNS will be described in Sections 4 and 5.

3.1 Simulation setup

The equations considered can be made nondimensional by using a characteristic velocity and length scale. With respect to the Ekman layer we consider the geostrophic wind velocity U_g and the Ekman layer depth $\delta_E = (2\nu/f)^{1/2}$, where f refers to the Coriolis parameter. By using these scaling variables we find the Ekman layer to be characterized by the nondimensional Reynolds number $Re = U_g\delta_E/\nu$. The Reynolds number determines the Rossby number $Ro = U_g/(f\delta_E)$ by the relation $Re = 2Ro$. Given the computational requirements for performing DNS we considered a DNS at $Re = 400$. For this Re , the computational DNS cost are still affordable. At the same time, the turbulence is sufficiently developed such that turbulence models can be tested: see Coleman et al. [18], Marlatt [20], and Shingai and Kawamura [22].

Table 1 compares the settings of our $Re = 400$ Ekman layer DNS with comparable DNS performed before. Here, the nondimensional numbers Re_1 and Ro_1 are defined by $Re_1 = U_g L_z/\nu$ and $Ro_1 = U_g/(fL_z)$. The domain lengths in x , y , and z directions are determined by L_x , L_y , and L_z , respectively. These lengths are normalized by $\delta = u^*/f$,

where $u^* = (\tau_w/\rho)^{1/2}$. The total shear stress at the wall is given by

$$\tau_w = \mu \sqrt{\left(\frac{\partial u}{\partial z}\right)^2 + \left(\frac{\partial v}{\partial z}\right)^2} \Bigg|_{z=0}, \quad (10)$$

where μ refers to the dynamic viscosity of the fluid. In addition, Table 1 refers to the number of grid points N_x , N_y , N_z in x , y , z directions, respectively, $u^+ = u/u^*$, $z^+ = zL_z/\nu$, and $x^+ = xL_x/\nu$.

The settings reported in Table 1 show that our $Re = 400$ DNS is very similar to the DNS of Shingai and Kawamura [22], for which the DNS data are available for comparisons [34]. The height of the domain is 2δ , a little larger than that used by [22]. DNS of Ekman layer turbulence at $Re = 400$ showed that the majority of the largest turbulent structures are captured when L_x and L_y are greater than 2δ (Coleman et al. [18], Waggy et al. [25]). In additional simulations (not shown) it was proven that the consideration of a larger horizontal domain using $L_x/\delta = L_y/\delta = 4$ did not affect the results reported here [35]. The simulation used a mesh resolution of $192 \times 192 \times 192$. The horizontal mesh is uniform, while the vertical mesh is clustered near the lower boundary using a hyperbolic tangent function. The first mesh point above the lower boundary is at $z^+ = 0.747$, there are approximately 14 points within the viscous sublayer ($z^+ \leq 10$), and approximately 144 points are within the depth of the turbulent boundary layer ($z \leq \delta$). The vertical mesh spacing at the upper boundary is characterized by $\Delta z^+ = 9.59$. We have $\Delta z_{max}/\delta_E = 0.37$ and $\Delta z_{max}/\delta = 0.03$. The horizontal resolution in wall units is $\Delta x^+ = \Delta y^+ = 3.47$. Given the higher order of the discretization method and the larger horizontal domain applied in [22], we conclude that the mesh spacings of our DNS and the DNS of [22] are comparable.

Table 1: DNS parameters: Our DNS compared with the DNS of Shingai and Kawamura [22], Waggy et al. [25], and Coleman et al. [18].

	Here	Ref. [22]	Ref. [25].	Ref. [18].
Re	400	400	400	400
Re_1	10,464	8,000	13,598	9,366
Ro	200	200	200	200
Ro_1	8	10	6	10
$L_x/\delta = L_y/\delta$	2	4.61	2	2
$N_x = N_y$	192	256	128	96
$\Delta x^+ = \Delta y^+$	3.47	6.09	5.28	7.06
L_z/δ	2	1.54	2.6	1.8
N_z	192	96	80	45
Δz^+	0.37–9.59	0.747–9.7	0.6–21.3	0.2–n/a

3.2 Numerical realization of DNS and LES

The simulation were performed by using the OpenFOAM CFD Toolbox [36], an unstructured finite-volume solver. The PISO algorithm was used for the pressure-velocity coupling in the Ekman layer simulations. The resulting algebraic equation for all the flow variables except pressure has been solved iteratively using a preconditioned bi-conjugate gradient method with a diagonally incomplete LU preconditioning at each time step. The convection term in the momentum equation was discretized using a second-order central difference scheme. The geostrophic wind is maintained through the adjustment of the driving pressure gradient in the momentum equation by the relation

$$2\mathbf{\Omega} \times (U_g, 0, 0) = -\frac{1}{\rho} \nabla p. \quad (11)$$

Here, $\mathbf{\Omega} = f\mathbf{k}/2$ refers to the rotation vector, where the unit vector in z direction is denoted by \mathbf{k} . In the case of LES, the Coriolis force and SGS viscosity are treated explicitly. The Poisson equation for the pressure was solved using an algebraic multi-grid (AMG) solver. When the scaled residual became less than 10^{-7} , the algebraic equation was considered to be converged. Time marching was performed using a second-order Crank–Nicolson scheme. Periodic boundary conditions have been employed along the streamwise and spanwise directions for all the flow variables. The nonslip condition is used on the bottom surface. At the top boundary, a slip-wall condition was specified for velocity and zero gradient conditions for all other variables.

For the DNS, the flow field was initialized by considering a laminar Ekman layer with superimposed random perturbations. Random perturbations drawn from a Gaussian distribution with zero mean and a variance of $(U_g/20)^2$ are used to simplify the transition to a turbulent state. The time step was based on the value of the CFL criterion, which was monitored during the simulation and remained below the limit $\Delta t(|u_c|/\Delta x_c)_{max} \leq 5 \times 10^{-3}$; u_c refers to the cell streamline velocity and x_c is the distance between adjacent cell centers. A dimensional time step of $\Delta t = 0.50$ was found to produce satisfactory results. This corresponds approximately to $\Delta t f = 5 \times 10^{-5}$, $\Delta t^+ = \Delta t u_*^2/\nu = 1.69 \times 10^{-2}$ and $\Delta t U_g/\delta = 7 \times 10^{-4}$. The simulation was run until the flow reached a statistically steady state based on the spatially averaged flow fields. The total simulation, terminated at 300,000 iterations, required approximately 120 CPU hours with 512 processors on 2.6-GHz Intel Xeon E5-2670 8-core processors at the NCAR-Wyoming Supercomputing Center. Ensemble

averaged flow field profiles were computed from $t_f = 32$ to $t_f = 57$ as temporal and horizontal averages.

LES at $Re = 400$ were performed on three grids, A1, A2 and A3. The values of numerical parameters are listed in Table 2. In the vertical direction, the first seven points are within approximately $z^+ = 10$. When starting a new simulation, an initial condition was generated by the laminar Ekman layer profile superimposed with perturbations obtained from a Gaussian distribution. All simulations were run for a time $2/f$ before averaging is started. Time averaging was then performed for a time period of $4\pi/f$. The time averages were additionally averaged over the homogeneous direction. The smallest time step that guaranteed stability was $\Delta t U_g/\delta_E = 0.0072$, or in term of the Coriolis parameter $\Delta t f = 3.6 \times 10^{-5}$.

Table 2: LES setup.

Case	N_x	N_y	N_z	L_x/δ	L_y/δ	L_z/δ	Δx^+	Δy^+	Δz^+
A1	96	96	96	2	2	2	7	7	0.74–18.93
A2	72	72	96	2	2	2	9.25	9.25	0.74–18.93
A3	48	48	96	2	2	2	14	14	0.74–18.93

3.3 Validation of DNS

A thorough analysis of the suitability of DNS results used here for the validation of LES can be found elsewhere [35]. Some relevant examples for the validation of our DNS are shown in the following, in particular in comparison to the DNS data of Shingai and Kawamura [22], which are available.

The surface shear angle β is computed by averaging the local shear angle,

$$\beta = \tan^{-1} \left(\frac{\overline{\partial V/\partial z}}{\overline{\partial U/\partial z}} \right). \quad (12)$$

The overbar refers here to a time averaged quantity that has been spatially averaged over horizontal planes. The averaged shear angle computed in our DNS was $\beta = 28.9^\circ$, which is considerably smaller than the laminar shear angle of 45° . A comparison with surface shear angles obtained in other DNS is provided in Table 3. It may be seen that there is a very good agreement. In particular, the deviation of our surface shear angle from $\beta = 28.65$ obtained by Shingai and Kawamura [22] is below 1%.

The mean velocity as function of z/δ and velocity hodograph obtained from our DNS and the DNS of Shingai and Kawamura [22] are shown in Figure 1. The laminar profiles are also shown for a comparison. It may

Table 3: DNS friction velocity and shear angle comparison.

Case	u_* / U_g	$\beta(\text{deg})$
Here	0.0647	28.9
[4]	0.0652	28
[24]	0.0654	28.6
[35]	0.0650	28.47
[34]	0.0650	28.65

be seen that there is an excellent agreement between our DNS and the DNS of Shingai and Kawamura [22].

Vertical turbulent stress profiles are presented in Figure 2. In particular, averaged turbulent normal and shear stresses obtained from our DNS are shown in (a)

and (b), respectively, in comparison to the DNS results of Shingai and Kawamura [22]. Our DNS results agree very well with the Reynolds stress results presented by [22] with the exception of the $\overline{u'v'}$ profile, which shows differences between the two DNS. It is of interest to note that Marlatt also reported a discrepancy of the $\overline{u'v'}$ profile obtained in his DNS [20] and the DNS of Coleman et al. [18] (a hump that is not seen in the results of Coleman et al.). The reason for these differences is not fully clear [20], it seems that the $\overline{u'v'}$ profile is very sensitive to minor grid and domain variations. Compared to the $\overline{u'v'}$ profile of the DNS of Shingai and Kawamura [22], it turns out that our $\overline{u'v'}$ profile (showing a pronounced peak structure for negative $\overline{u'v'}$ values) agrees much better with the structure of $\overline{u'v'}$ profiles obtained by both

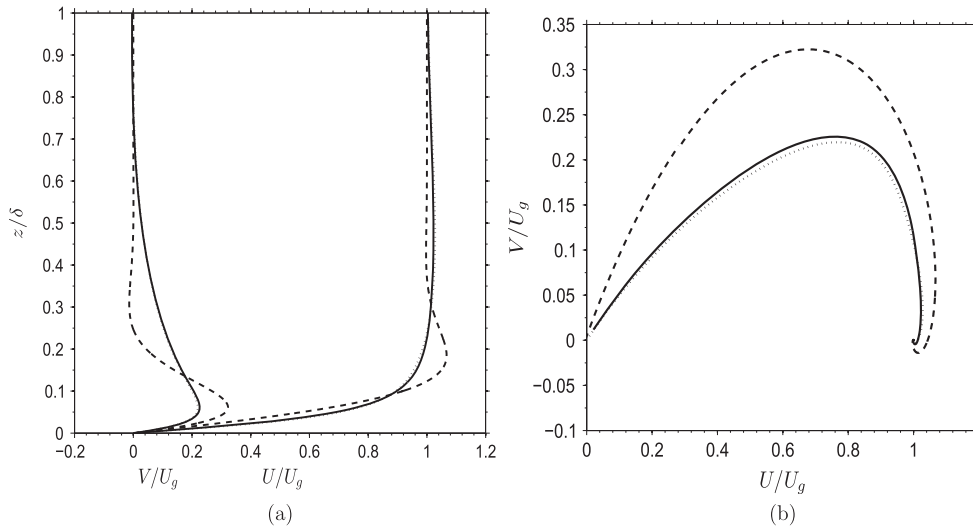


Figure 1: The mean velocities and velocity hodograph are shown in (a) and (b). Lines: our DNS (solid line), laminar profile (dashed line), DNS of Shingai and Kawamura [34] (dotted line).

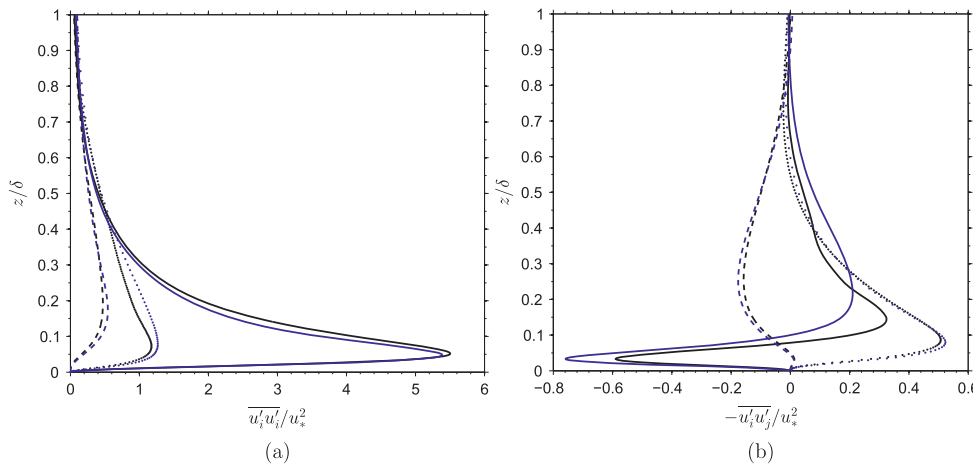


Figure 2: Stress profiles, (a) Reynolds normal stresses: $\overline{u'u'}/u_*^2$ (solid line), $\overline{v'v'}/u_*^2$ (dotted line), $\overline{w'w'}/u_*^2$ (dashed line), (b) Reynolds shear stresses: $-\overline{u'v'}/u_*^2$ (solid line), $-\overline{u'w'}/u_*^2$ (dotted line), $-\overline{v'w'}/u_*^2$ (dashed line). Our DNS: in black, Shingai and Kawamura DNS [34]: in blue.

Marlatt [20] and Coleman et al. [18] Overall, given the very good agreement of our DNS and the DNS of Shingai and Kawamura [22] with respect to mean velocities and all the other stress components, our conclusion is that both DNS agree at least reasonably well.

4 Ekman layer simulations: model stability features

Let us consider first the stability features of the original DSM, stabilized DSM, and LDM before analyzing the model performance with respect to turbulence simulations in Section 5. In particular, we will compare the tendency of models to develop computational instabilities via the excessive generation of negative model parameter values (see the explanations in Section 4.3). This will be done in the following subsections by considering instantaneous model parameters, the PDF of model parameters, and the temporal correlation function of model parameters, respectively.

4.1 Dynamic model parameter variations

Instantaneous local values of C_S obtained by the original DSM, stabilized DSM, and LDM are shown in Figure 3 at $x^+ = 333$, $y^+ = 333$ in streamwise and spanwise directions and $z^+ = 2.6$ and $z^+ = 87.6$, respectively, in vertical direction. The latter two vertical positions correspond to distances in the viscous layer very close to the wall and in the region far away from the wall where the mean velocity begins to level off (see Figure 6), respectively.

The original DSM model parameter is obtained from eq. (5) by post processing the results obtained by using the stabilized DSM. Figure 3(b) shows that there are huge fluctuations of C_S . The mean value of C_S near and away from the wall is -0.0015 and 0.0164 , respectively. The stabilized DSM C_S is the value calculated by expression (7). It may be seen that the range of C_S fluctuations is significantly smaller than given by the original DSM. The mean of C_S is -0.0014 near the wall and 0.0061 away from the wall, respectively. The LDM C_S is the value calculated by expression (8). Compared to the original DSM and stabilized DSM, it may be seen that the C_S curve shows a much smaller range of variations. The mean value of C_S near and away from the wall is 0.0000 and 0.0034 , respectively.

The comparison of the three C_S variations considered shows that the LDM represents a much more effective way of stabilizing the dynamic model parameter C_S

compared to the stabilized DSM. The comparison of Figure 3(b) and 3(f) indicates that the basic variation of C_S provided by the LDM is similar to the variation of C_S in the original DSM with the exception that very large negative and positive deviations from the mean are suppressed.

4.2 Dynamic model parameter PDFs

A much more complete view of the behavior of dynamic model parameters is obtained by looking at the PDF of C_S . These plots are shown in Figure 4 for the original DSM, stabilized DSM, and LDM at $x^+ = 333$, $y^+ = 333$ in streamwise and spanwise directions and $z^+ = 2.6$ and $z^+ = 87.6$, respectively, in vertical direction. The PDFs were calculated by using 2 million samples. This is sufficient for the calculations of PDFs that are basically unaffected by the number of samples applied [37]. The filter size used for the PDF calculations of the LDM near and away from the wall are 10^{-4} and 0.0009 , which differ from the corresponding values 0.004 and 0.0009 used for the PDF calculation for the original DSM and stabilized DSM.

A basic observation is that all PDFs differ significantly from the corresponding C_S PDF found in channel flow, which has approximately a uniform PDF shape [16]. Away from the wall at $z^+ = 87.6$, all the PDFs show that the appearance of positive C_S values is more likely. The asymmetry of C_S PDFs can be attributed to the rotating flow considered. As expected, the stabilized DSM PDF has a smaller range of C_S values than the original DSM. A further reduction of the range of C_S values is given by using the LDM.

Significant differences between the models considered can be seen close to the wall at $z^+ = 2.6$. The original DSM PDF shows the reason for the computational instability generated by this model: there is a high probability of large negative C_S values. This problem can be significantly reduced by using the stabilized DSM model that reduces the range of possible negative C_S values. However, the stabilized DSM model shows (in contrast to the behavior of all PDFs far away from the wall) that negative C_S values are more likely than positive C_S values. The LDM PDF features are very different. First, this model reduces the range of C_S variations by a factor of about 50. Second, in line with the behavior of all PDFs far away from the wall, the probability of positive C_S values is higher than the probability of negative C_S values.

In summary, the use of the stabilized DSM has to be preferred compared to the original DSM because

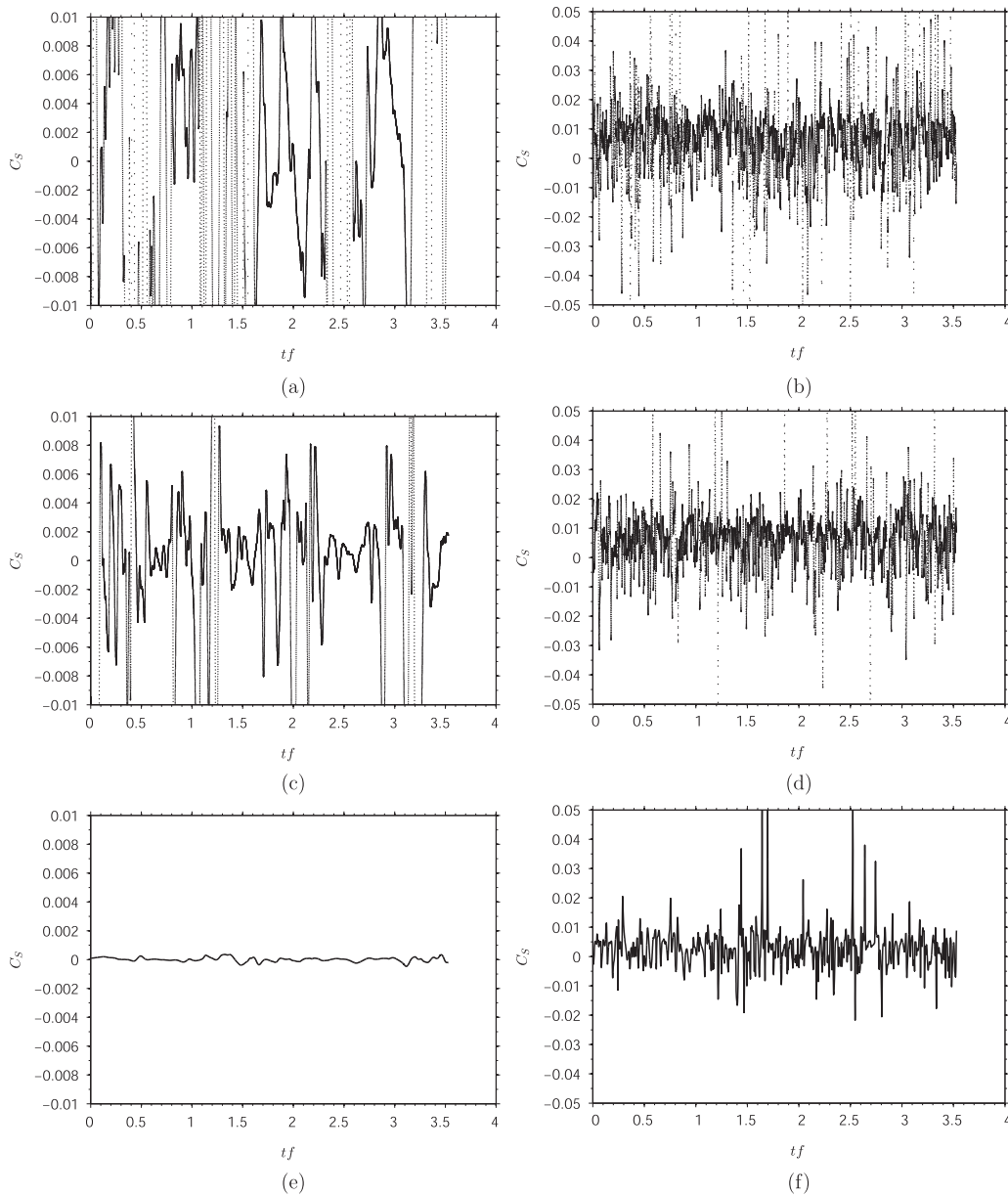


Figure 3: Case A1 model coefficient $C_S(t)$. First row: original DSM, second row: stabilized DSM, third row: LDM. Left and right pictures show $C_S(t)$ at $(x^+, y^+, z^+) = (333, 333, 2.6)$ and $(x^+, y^+, z^+) = (333, 333, 87.6)$, respectively.

it significantly reduces the source of computational instabilities. However, the LDM is much more effective than the stabilized DSM with respect to the reduction of the range of negative C_S values. In addition, the LDM probability for finding positive C_S values is higher than the probability for finding negative C_S values. This is a desired physical feature. According to $\tau_{ij}^d = -2C_S\Delta^2|\tilde{S}_{ij}|$, this means that τ_{ij}^d is more frequently correlated to $-\tilde{S}_{ij}$, which corresponds to the local equilibrium model [16].

4.3 Dynamic model parameter correlations

The temporal autocorrelation function (ACF) of C_S may be relevant to the explanation of computational instabilities. Possibly, this instability can be traced to the fact that C_S has a large auto-correlation time [11]. Therefore, if C_S becomes negative in some regions, it may remain negative for excessively long periods of time during which the exponential growth of the local velocity fields, associated with a negative eddy viscosity, causes a divergence of the

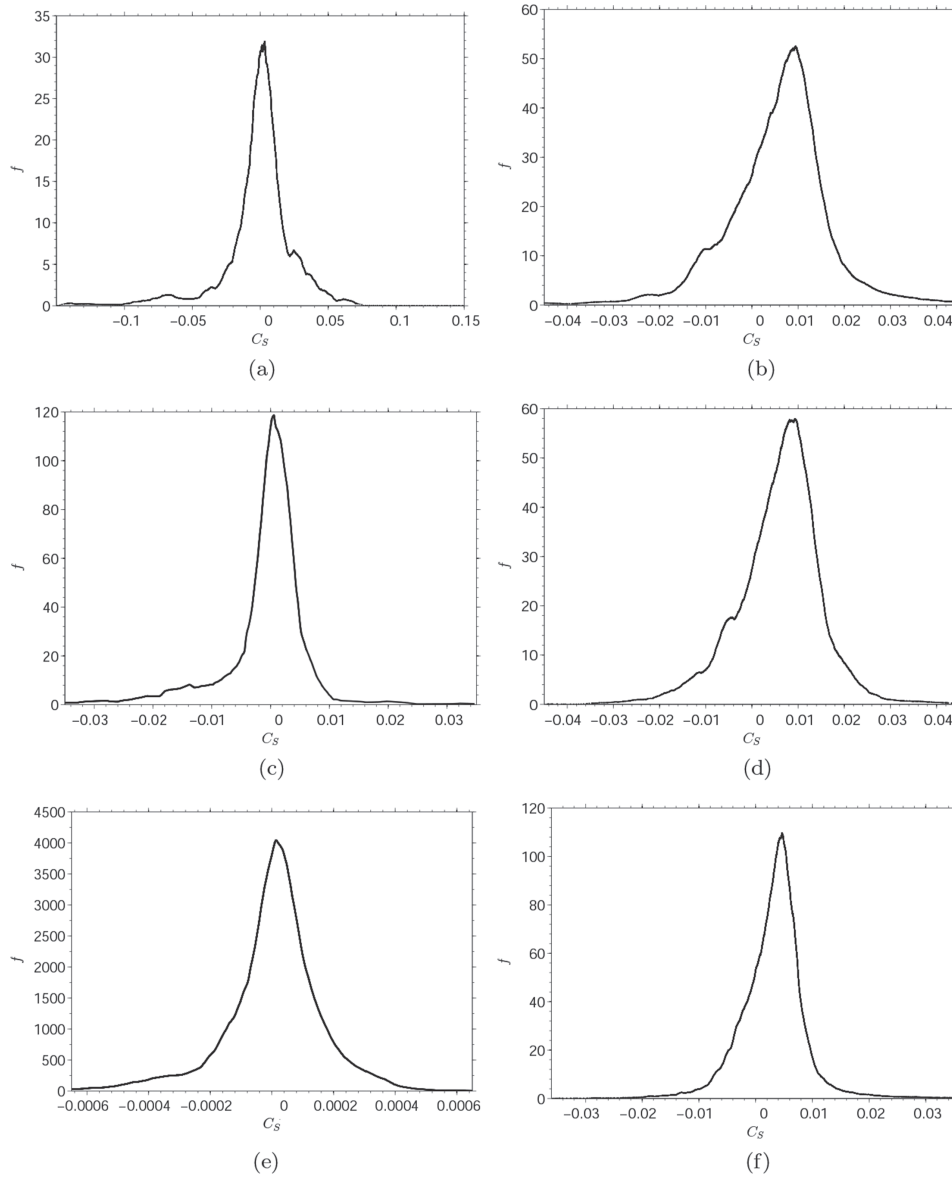


Figure 4: Case A1 PDF of $C_S(t)$. First row: original DSM, second row: stabilized DSM, third row: LDM. Left and right pictures show the PDF at $(x^+, y^+, z^+) = (333, 333, 2.6)$ and $(x^+, y^+, z^+) = (333, 333, 87.6)$, respectively.

total energy. To get a better insight into this question we consider the ACF implied by the original DSM, stabilized DSM, and LDM. Here, for any variable x_i where $i = 1, N$, the ACF r_k for observations separated by k time steps is defined by (\bar{x} refers to the mean value)

$$r_k = \frac{\sum_{i=1}^{N-k} (x_i - \bar{x})(x_{i+k} - \bar{x})}{\sum_{i=1}^N (x_i - \bar{x})^2}. \tag{13}$$

The C_S ACF is shown in Figure 5 for the original DSM, stabilized DSM, and LDM for time lags from 1 to 250. More than 40,000 samples were used for the ACF calculations.

Far away from the wall at $z^+ = 87.6$, the original DSM ACF indeed shows a correlation of negative C_S values over more than 100 time lags. In conjunction with the fact that this negative correlation is much smaller for the stabilized DSM, this fact supports the view of Ghosal et al [11] described above. However, even the stabilized DSM shows a small region of negative correlation over about 35 time lags. The continuous correlation decay of the original DSM from positive to negative values indicates a stable mechanism of generating negative C_S values: such ACF structures are known from turbulent boundary layers close to the wall, they reflect alternating areas of

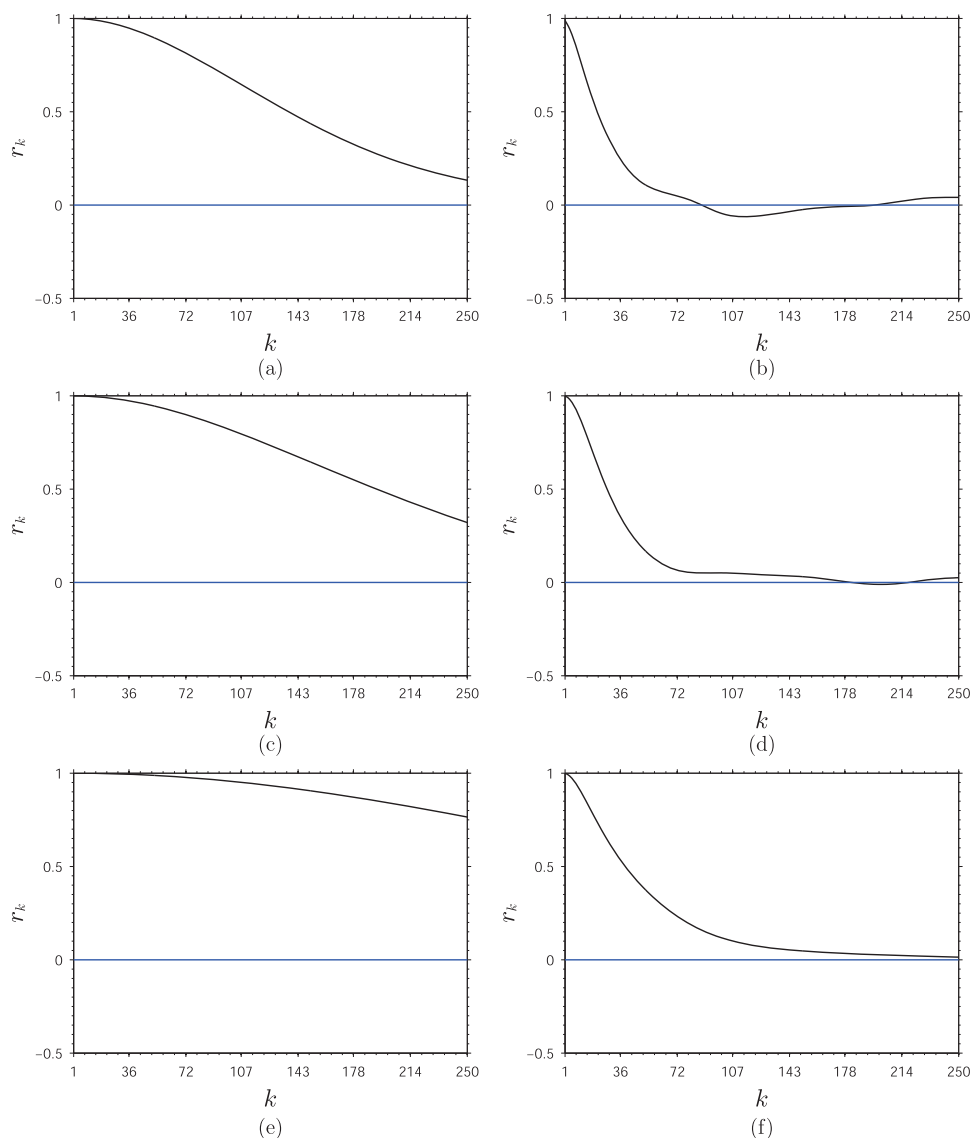


Figure 5: Case A1 ACF. First row: original DSM, second row: stabilized DSM, third row: LDM. Left and right pictures show the ACF at $(x^+, y^+, z^+) = (333, 333, 2.6)$ and $(x^+, y^+, z^+) = (333, 333, 87.6)$, respectively.

positive and negative velocity fluctuations (streaks) [38]. The corresponding LDM features are very different. First, there is no negative correlation. Second, a very interesting fact is that the positive LDM C_S values are much longer correlated than the original DSM and stabilized DSM values. This supports the view that the proportionality assumption expressed by the LDM relation $L_{ij}^d = -C_S M_{ij}$ is a better model assumption than the assumptions used in the original and stabilized DSM: a longer characteristic correlation time means that L_{ij}^d and M_{ij} are longer correlated.

Close to the wall at $z^+ = 2.6$, we observe the following regarding the three ACFs. All three correlation values are much higher compared to the ACFs at $z^+ = 87.6$. This fact

is supported by Figure 3 which also shows the correlation of C_S values. The reason for the higher ACFs is that the C_S values at $z^+ = 2.6$ are much smaller than the C_S values at $z^+ = 87.6$. There is a much smaller decorrelation effect caused by the structure of near-wall motions: this difference is implied by the existence of long, elongated streaks (which do not much promote a decorrelation of velocities) combined with a smaller amount of decorrelating small-scale motions than seen well away from the wall.

To summarize, both the original DSM and stabilized DSM suffer from the problem of a relatively long period of negative correlations that generate computational instabilities, although this period is much smaller for

the stabilized DSM model. On the other hand, the LDM is not affected at all by this problem.

5 Ekman layer simulations: model performance evaluation

Next, the performance of the stabilized DSM and LDM with respect to turbulence simulations will be evaluated. The original DSM is not applicable in such simulations because it produces computational instabilities. The performance evaluation will be done with respect to mean fields in Section 5.1, instantaneous velocity fields in Section 5.2, and grid effects on mean fields, stresses, and instantaneous velocity fields in Section 5.3.

5.1 Mean fields and Reynolds stresses

The mean velocity profile $Q^+ = [(U^+)^2 + (V^+)^2]^{1/2}$ for the models considered is shown as a function of the wall-normal distance z^+ in Figure 6. The mean velocity profiles of the LDM and stabilized DSM agree very well with the DNS data. The SM mean velocity profile follows the DNS data in the near wall region but not in the log-law region: its slope is slightly too small. For $z^+ > 50$ the SM slightly overestimated the mean velocity. The individual components of the mean horizontal velocity are shown in the hodograph. The agreement of the LDM with DNS is excellent, the stabilized DSM over-estimates the cross-stream velocity, and the SM also shows deviations from the DNS data.

Turbulence intensity profiles are shown in Figure 7: $u_{rms}/|U|$, $v_{rms}/|U|$, and $w_{rms}/|U|$ refer to the normalized diagonal elements of the total stress tensor given by the

sum of resolved and modeled stresses. The LDM and stabilized DSM profiles of spanwise and streamwise turbulence intensities agree very well with the DNS. On the

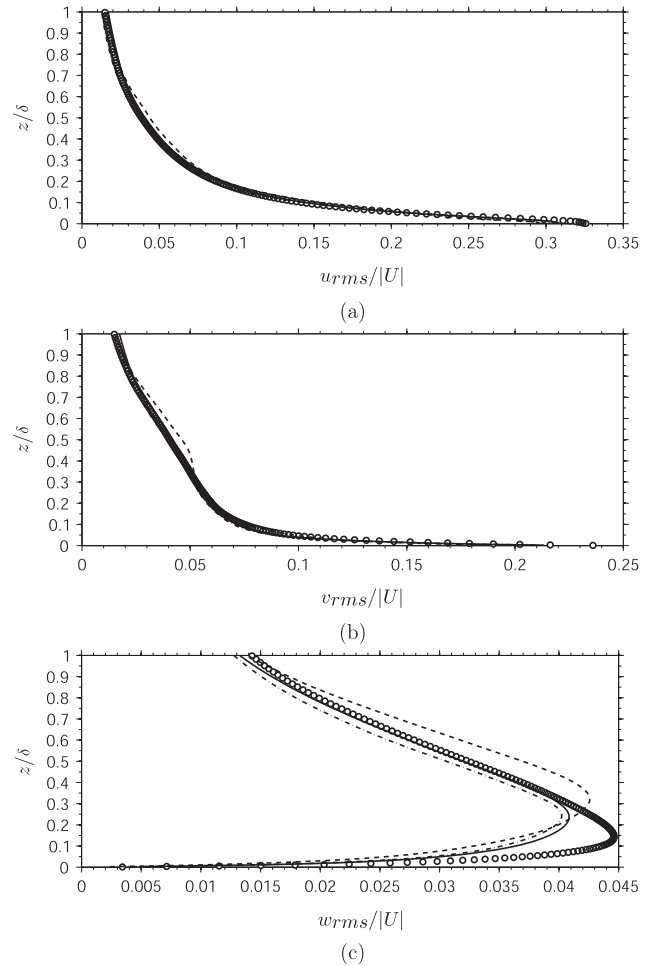


Figure 7: Case A1 turbulence intensities $u_{rms}/|U|$, $v_{rms}/|U|$, $w_{rms}/|U|$ in (a), (b), and (c), respectively: DNS (open circles), LDM (solid line), DSM (dot-dashed line), SM (dashed line).

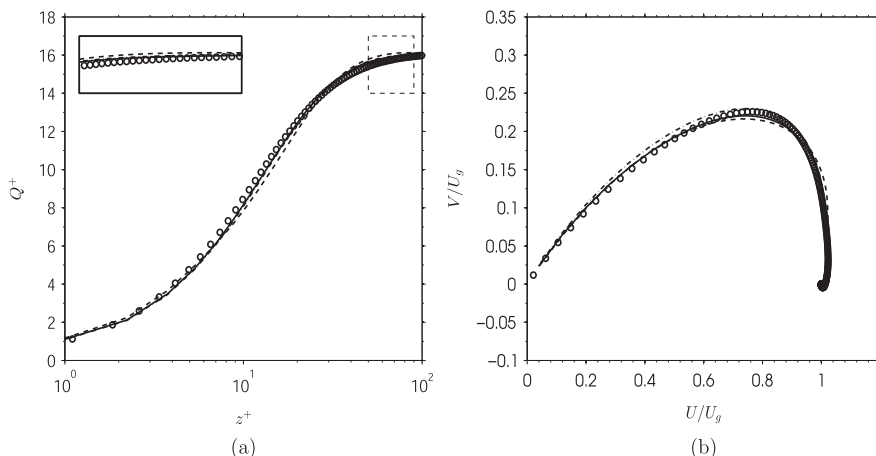


Figure 6: Case A1 mean-velocity profile (a) and hodograph (b): DNS (open circles), LDM (solid line), stabilized DSM (dot-dashed line), SM (dashed line).

other hand, the SM profile shows a significant mismatch with the DNS data away from the wall. The wall normal components obtained by the stabilized DSM and LDM, which are shown in Figure 7(c), show a relatively good agreement with the DNS data. The peak value and its position are not fully captured. Again, the SM profile shows deviations from the DNS data that are much more pronounced than the deviations of the stabilized DSM and LDM. In particular, the peak position of $w_{rms}/|U|$ is incorrectly predicted. Nevertheless, it has to be noted that the $w_{rms}/|U|$ values are very small compared to $u_{rms}/|U|$ and $v_{rms}/|U|$ values: the peak value of $w_{rms}/|U|$ is about 14% of the peak value of $u_{rms}/|U|$. If $w_{rms}/|U|$ values are plotted in a scale equal to the range of $u_{rms}/|U|$ variations, there would be hardly any observable difference between DNS data, LDM and stabilized DSM predictions.

The latter view is confirmed in terms of Figure 8, which shows LDM, stabilized DSM, and SM vertical profiles of the turbulent kinetic energy. Regardless the little discrepancies seen in Figure 7(c), the LDM and stabilized DSM profiles show an excellent agreement with the DNS data. The SM profile shows discrepancies with the DNS data that are caused by the deviations seen in Figure 7(a) and 7(b). Figure 8 also addresses the question about the ratio of resolved to modeled stresses. With respect to the LDM and stabilized DSM, the modeled stress contributions are approximately zero. Otherwise, regarding the SM, it may be seen that there is a small modeled stress contribution close to the wall.

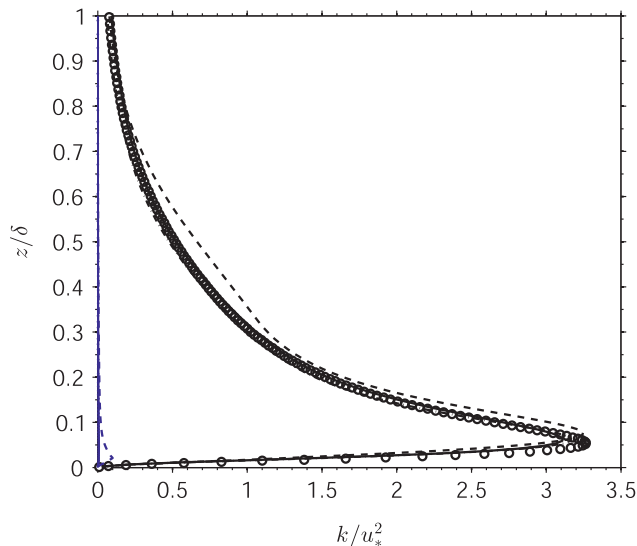


Figure 8: Case A1 turbulent kinetic energy: DNS (open circles), LDM (solid line), stabilized DSM (dot-dashed line), SM (dashed line). The total turbulent kinetic energy is shown in black, the modeled turbulent kinetic energy is shown in blue.

The question about the relevance of modeled stress contributions is also addressed in terms of Figure 9. Here, $-\overline{u'w'}/u_*^2$ and $-\overline{v'w'}/u_*^2$ refer to the resolved components of nondiagonal stress components, whereas $-B_{xz}/u_*^2$ and $-B_{yz}/u_*^2$ refer to the corresponding total components. The LDM and stabilized DSM profiles show a behavior corresponding to the features seen in Figure 8. There is a relatively good agreement with DNS data (the LDM predicts $-\overline{u'w'}/u_*^2$ slightly better than the stabilized DSM), and the modeled stress contributions have a negligible influence. The SM features are very different. With respect to the resolved stress contributions there is a comparable agreement with DNS data as given for the LDM and stabilized DSM. Nevertheless, the inclusion of modeled stress contributions leads to an incorrect prediction of total stresses given by the SM. In particular, the near wall behavior is incorrectly simulated as a consequence of the damping function applied. It is interesting to see that this conclusion applies to both stress components considered (according to the concept of designing damping functions one might have expected that the shear stress $-B_{xz}/u_*^2$ does not significantly suffer from such shortcomings). The SM damping function considered is similar to detached eddy simulation (DES) methods [27], which are known to have a performance that is usually affected by the grid. If the SM shortcoming would be mainly caused by the grid, then it would be plausible to see a corresponding effect of grid variations. But Figure 17 shown below does not reveal such an effect: the SM shortcomings are almost the same on several grids considered. Therefore, it is likely that the poor SM performance is caused by the fact that standard concepts of designing damping functions are not applicable to flows that are significantly affected by rotation [39], dynamic LES are needed to overcome this problem.

5.2 Instantaneous velocity fields

After considering the performance of the models considered with respect to mean flow properties, i.e., mean velocities and Reynolds stresses, we will study now such differences for instantaneous velocities. The latter leads to valuable conclusions for channel flow simulations [16], and the same can be expected here. Contours of the instantaneous velocity fluctuations u' , v' and w' in horizontal planes $z^+ = (2.6, 87.6)$ are shown in Figures 10–11 at $tf = 2.3$. The contour interval is $\Delta = 0.15$ for all cases except w' at $z^+ = 2.6$, where $\Delta = 0.02$.

The near wall instantaneous velocity structures at $z^+ = 2.6$ are shown in Figure 10. With respect to u'

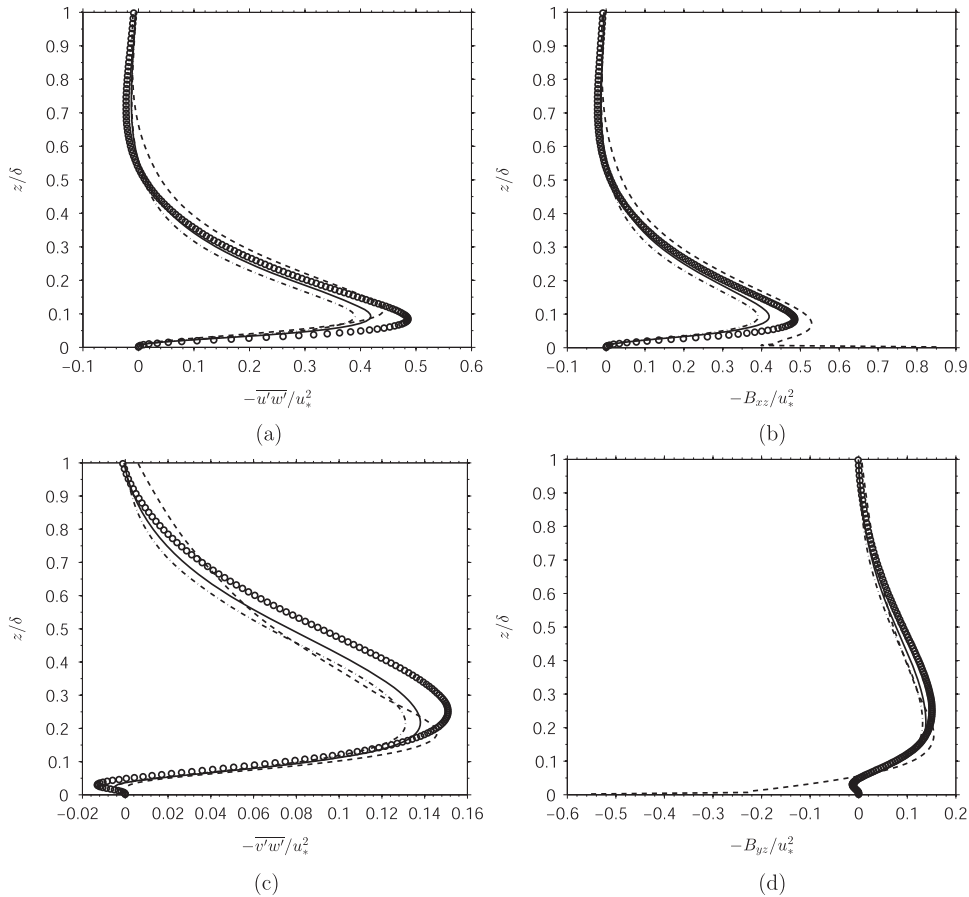


Figure 9: Case A1 nondiagonal stress components. The resolved component $-\overline{u'w'}/u_*^2$ and the corresponding total stress $-B_{xz}/u_*^2$ are shown in (a) and (b), respectively. The resolved component $-\overline{v'w'}/u_*^2$ and the corresponding total stress $-B_{yz}/u_*^2$ are shown in (c) and (d), respectively. DNS (open circles), LDM (solid line), stabilized DSM (dot-dashed line), and SM (dashed line) results.

fluctuations, we see in DNS the typical long elongated structures close to a wall [16]. These streaks are very long, they continue throughout the whole domain. In contrast to channel flow we see a tilting of these structures, which is implied by the Coriolis force. The LDM is capable of producing approximately the same streaky structures seen in DNS. The stabilized DSM features are relatively similar with the exception that the fine scale structure is not so well resolved as given by the LDM (we observe larger areas of positive and negative velocity fluctuations). The SM features are very different. First of all, the SM is not capable of producing structures that reveal the same tilting as seen in DNS. Instead, the structures indicate a tilting in the opposite direction. In addition, areas of positive and negative fluctuations are merged to larger regions than seen in DNS. The corresponding v' fluctuations show significant similarities to the behavior of u' fluctuations. In particular, the DNS, LDM, and stabilized DSM features do hardly show differences to the corresponding u' structures. With respect to the SM

model we see again a tilting in the opposite direction to the DNS tilting. The areas of positive and negative velocity fluctuations are even much larger than with respect to the u' fluctuations. The corresponding w' fluctuations show a different behavior than the u' and v' fluctuations. In DNS, we see more small scale structures. This is caused by the fact that w' fluctuations are much smaller than u' and v' fluctuations: see Figure 7(c). A tilting of these structures also can be seen. Both, the LDM and stabilized DSM are able to predict these velocity structures very well. The use of the SM produces the same problems as seen with respect to u' and v' fluctuations.

The instantaneous velocity structures far away from the wall at $z^+ = 87.6$ are shown in Figure 11. Again, u' and v' fluctuations show relatively similar structures such that their features will be discussed together. The DNS features differ from those seen at $z^+ = 2.6$ by two facts. First, the tilting is stronger and in the opposite direction. Second, we observe larger structures. The latter observation is a typical feature for turbulence away from the wall

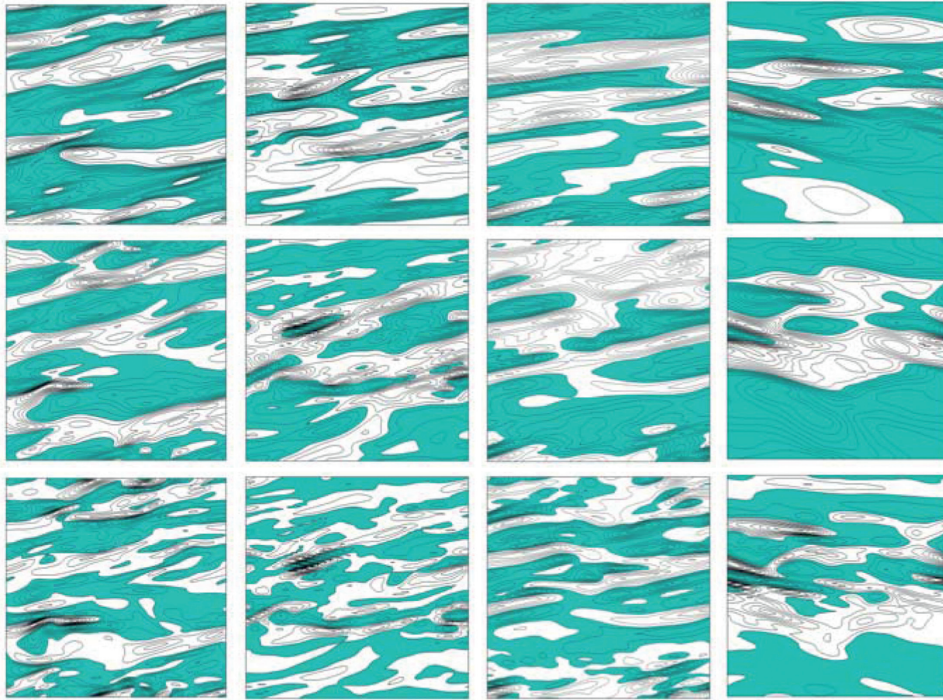


Figure 10: Case A1 velocity fluctuations at $z^+ = 2.6$: negative regions are colored. From left to right: DNS, LDM, stabilized DSM, SM. First row: u'/u_* , second row: v'/u_* , third line: w'/u_* .

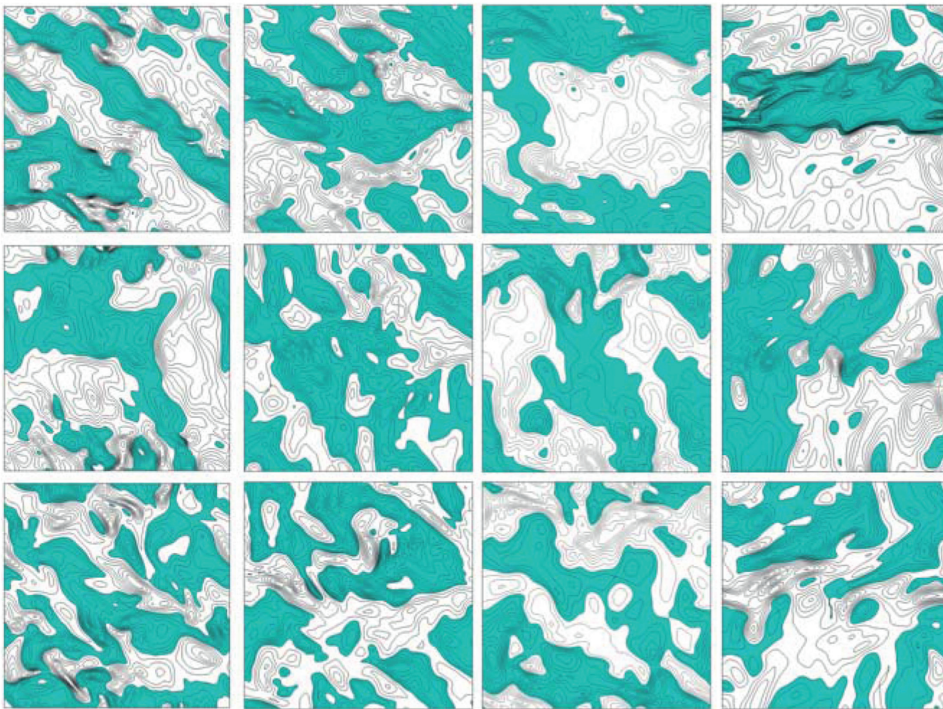


Figure 11: Case A1 velocity fluctuations at $z^+ = 87.6$: negative regions are colored. From left to right: DNS, LDM, stabilized DSM, SM. First row: u'/u_* , second row: v'/u_* , third line: w'/u_* .

(the turbulent eddies increase with a growing wall distance), which is also seen in channel flow simulations [16]. Again, the LDM produces the same features as seen in DNS. With respect to the stabilized DSM, there are clear differences to DNS. First, there is no evidence for a tilting of instantaneous structures. Second, the areas of positive and negative velocity fluctuations are much larger, this means the fine scale structure of turbulence is incorrectly represented. The SM suffers from exactly the same shortcomings as the stabilized DSM. With respect to w' fluctuations there is not a big difference to the features seen at $z^+ = 2.6$ with the exception of the fact that the tilting is stronger and in the opposite direction. The LDM and stabilized DSM are able to produce almost the same structures as seen in DNS. The tilting provided by the SM is again incorrect.

To summarize, we find that the LDM produces turbulence structures close and away from the wall as seen in DNS. In contrast to that, the SM produces incorrect turbulence structures with the opposite tilting, which are way too large. The behavior of the stabilized DSM depends on the wall distance. Close to the wall it produces acceptable turbulence structures that agree, basically, with DNS. Away from the wall the stabilized DSM suffers from exactly the same shortcomings as the SM.

5.3 Grid effects

The analysis of the grid dependence of the performance of the models considered is definitely relevant. In

particular, there is the question of how the models respond to a systematic coarsening of grids. Three grids, the A1, A2, and A3 grids specified in Table 2, will be used to address this question. These grids refer to a coarsening only in homogeneous directions to maintain a similar grid topology.

Instantaneous streamwise velocity fluctuations u' are shown for the three grids considered at $tf = 2.3$ close ($z^+ = 2.6$) and away from the wall ($z^+ = 87.6$) for the LDM, stabilized DSM, and SM in Figures 12–14, respectively. With respect to both $z^+ = 2.6$ and $z^+ = 87.6$, the use of the LDM shows that instantaneous structures merge and become larger with an increasing grid coarsening. This is exactly the expected trend: the grid coarsening results in large RANS-type structures involving less and less fine scale structures. Basically, the stabilized DSM shows the opposite trend, also for both $z^+ = 2.6$ and $z^+ = 87.6$. The grid coarsening does not reduce the appearance of fine scale structures. For example, the comparison of results on the A1 and A2 grids shows that there are more structures on the A2 grid than on the A1 grid. The reason for this unphysical behavior is the DSM approach to stabilize the original DSM via a local averaging over cell faces. The concept to provide C_S as superposition of spatially separated contributions (different face contributions) corresponds to the inclusion of spatial correlations of fluctuations (the same instantaneous values are used to obtain C_S at several spatially separated points). On coarse grids, such correlations can promote the development of correlated LES-type motions. On the other hand, this influence can be expected to be of

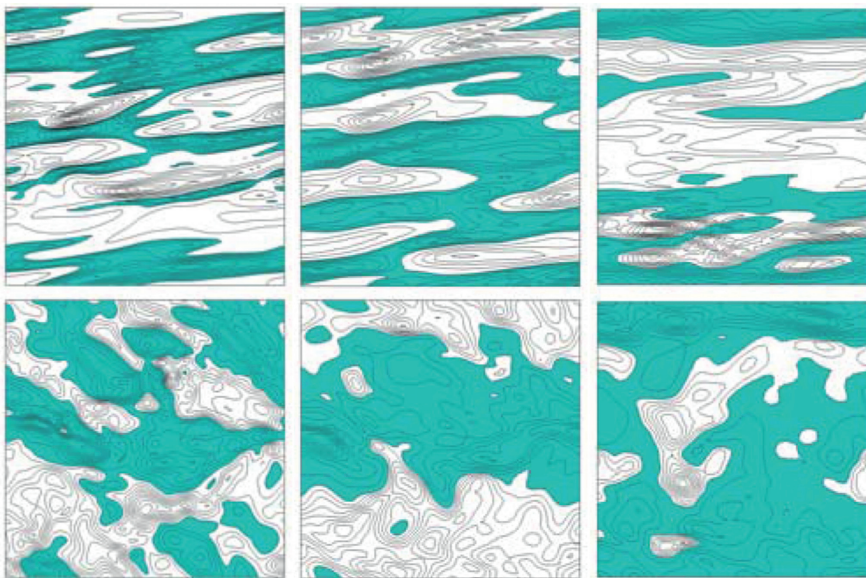


Figure 12: LDM u'/u_* velocity fluctuations. From left to right: A1, A2, and A3 grid results, respectively. First row: u'/u_* at $z^+ = 2.6$, second row: u'/u_* at $z^+ = 87.6$.

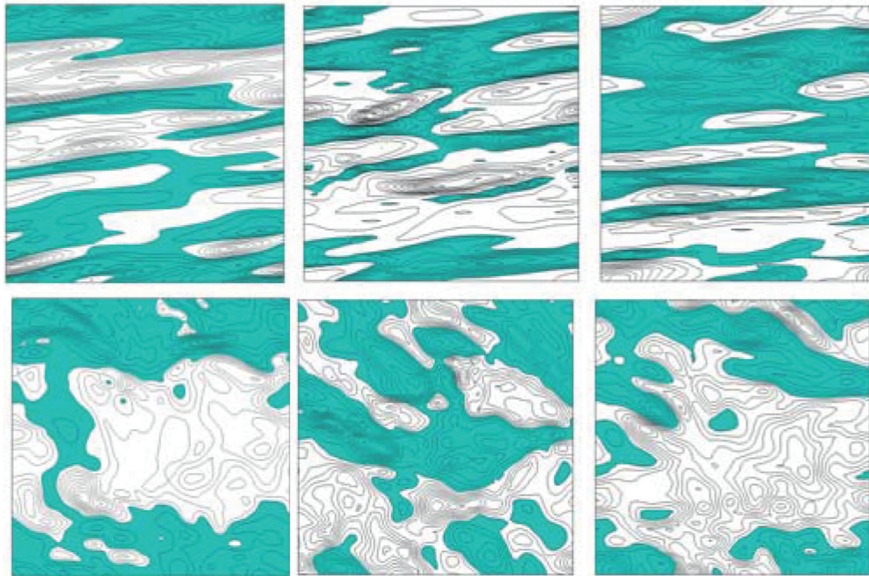


Figure 13: Like Figure 12 but for the stabilized DSM.

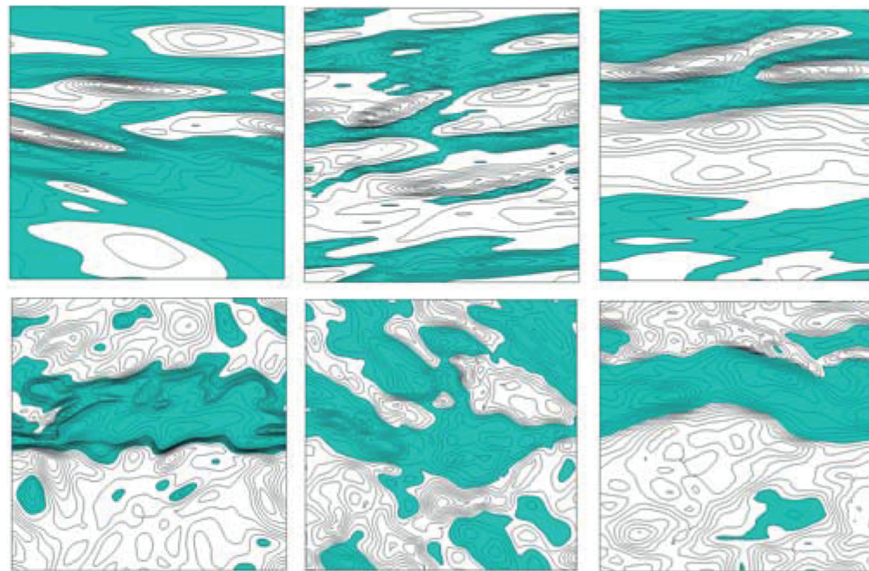


Figure 14: Like Figure 12 but for the SM.

minor relevance on sufficiently fine grids that enable the resolution of large-scale motions. The term face-average-induced-correlations will be used below to refer to correlations caused by the stabilized DSM averaging concept. With respect to the SM behavior it seems to be difficult to derive a clear conclusion. The comparison of results on the A1 and A3 grids supports the view that the SM behavior is similar to the LDM behavior, this means the SM behaves as expected.

Figure 15 demonstrates the effect of grid coarsening on LDM mean field predictions. The mean velocity is hardly affected by the grid coarsening considered, but stress components are affected. Overall, the grid effect corresponds to expectations: a gradual grid coarsening leads to a gradual reduction of turbulent stresses. It is of interest to see that the relatively coarse A2 grid does not affect the turbulence intensities $u_{rms}/|U|$ and $v_{rms}/|U|$. The A2 grid effect on $w_{rms}/|U|$ is small regarding the

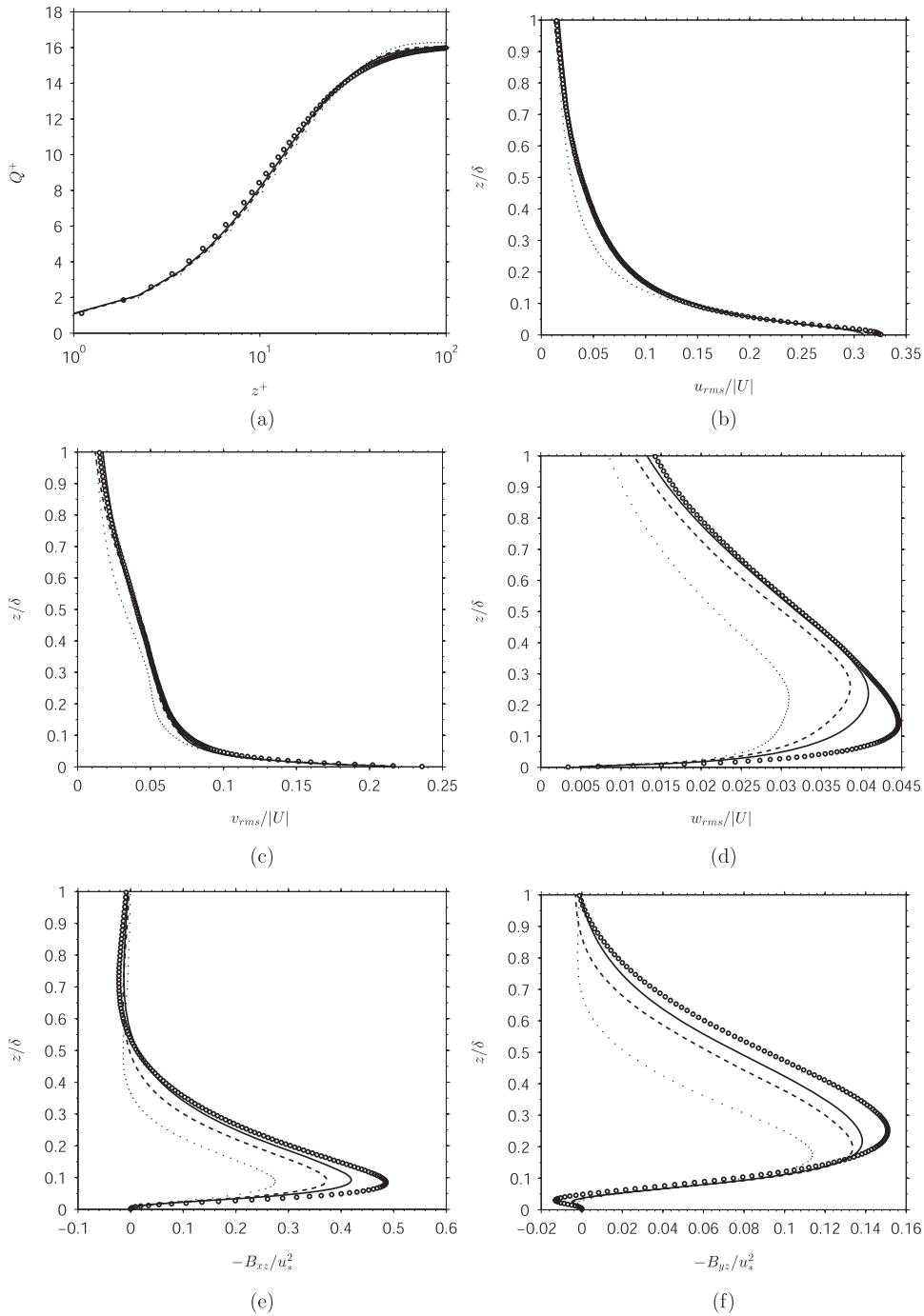


Figure 15: LDM: (a) Q^+ , (b) $u_{rms}/|U|$, (c) $v_{rms}/|U|$, (d) $w_{rms}/|U|$, (e) $-B_{xz}/u_*^2$, (f) $-B_{yz}/u_*^2$. DNS (open circles); A1 grid (solid line), A2 grid (dashed line), and A3 grid (dotted line) results.

fact that $w_{rms}/|U|$ is very small compared to $u_{rms}/|U|$ and $v_{rms}/|U|$ (the plot of $w_{rms}/|U|$ in the scale of $u_{rms}/|U|$ variations would hardly show any difference). The very coarse A3 grid is obviously too coarse to enable very accurate turbulence intensity predictions. As it can be expected, the grid effect on $-B_{xz}/u_*^2$ and $-B_{yz}/u_*^2$ is

slightly stronger, but the A2 grid results are at least comparable with the A1 grid results.

Figure 16 shows corresponding grid effects on stabilized DSM predictions. As found for the LDM, the mean velocity profile is basically unaffected by the grid coarsening applied. The grid effect on the turbulence

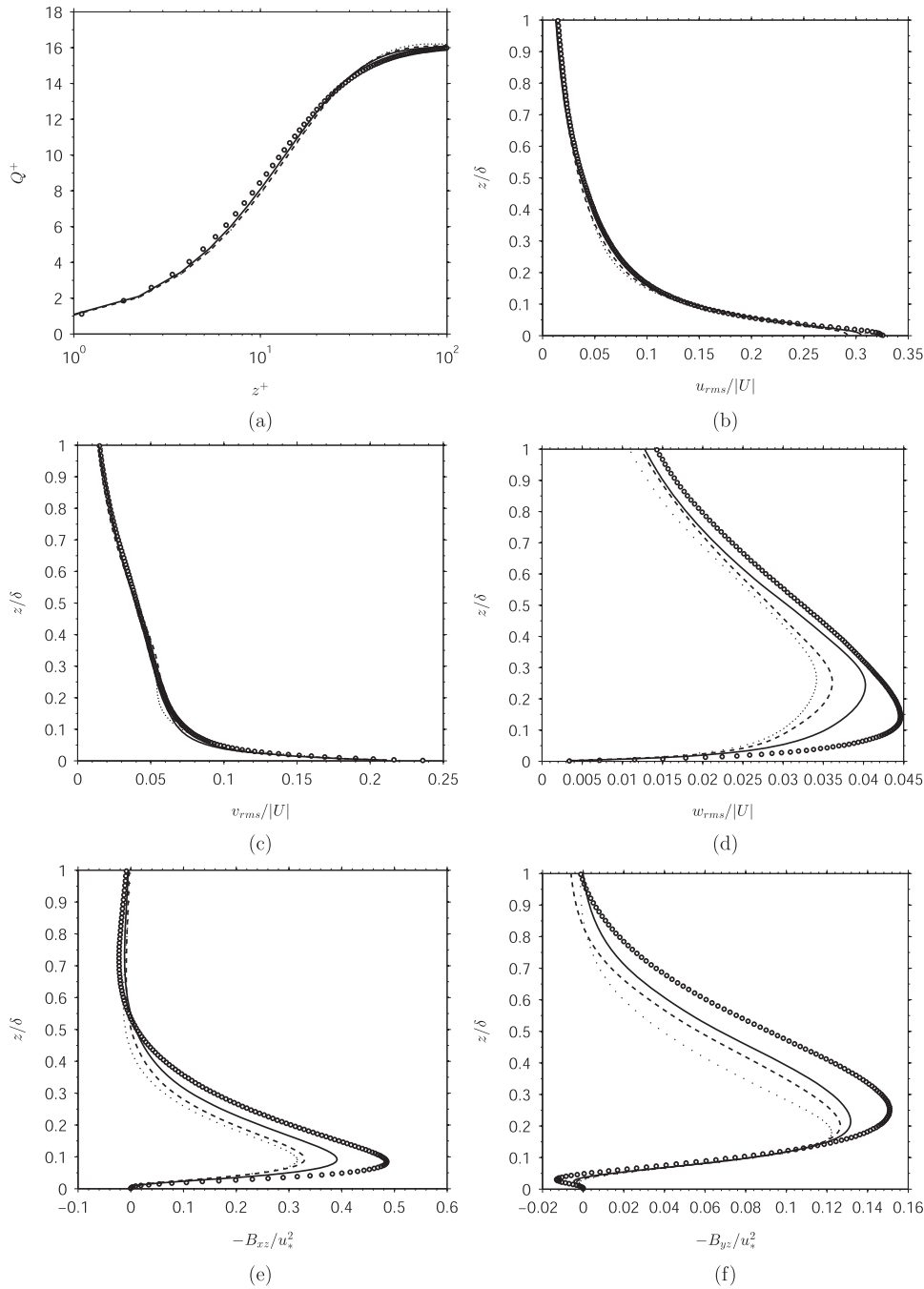


Figure 16: DSM: (a) Q^+ , (b) $u_{rms}/|U|$, (c) $v_{rms}/|U|$, (d) $w_{rms}/|U|$, (e) $-B_{xz}/u_*^2$, (f) $-B_{yz}/u_*^2$. DNS (open circles); A1 grid (solid line), A2 grid (dashed line), and A3 grid (dotted line) results.

intensities $u_{rms}/|U|$ and $v_{rms}/|U|$ is less pronounced than given for LDM predictions. In particular, the A3 grid still provides predictions that are rather similar to the predictions on the finer A2 and A1 grids. This fact reflects an unphysical behavior, a significant grid coarsening needs to result in a noticeable reduction of resolved stress. With respect to this question, it is worth noting that the total

stresses shown in Figure 16 are almost identical to the resolved stresses, see Figure 8. An explanation for this stabilized DSM model behavior can be obtained by taking reference to the corresponding plots of instantaneous velocities. The effect of face-average-induced-correlations described above, which are implied by the DSM stabilization concept, accidentally improves model predictions

because of the promotion of LES-type motions. However, it is relevant to note that this is a random effect. For another flow or at another Reynolds number, this effect may cause significant negative effects on turbulence predictions.

Figure 17 shows corresponding grid effects on SM predictions. These figures reveal significant shortcomings

of SM predictions. The inaccurate prediction of the mean velocity using the A1 grid becomes more pronounced on coarse grids. Also the prediction of turbulence intensities suffers from significant problems, see, for example, the $w_{rms}/|U|$ predictions on all three grids. The total stress components $-B_{xz}/u_*^2$ and $-B_{yz}/u_*^2$ suffer from the problems discussed with respect to Figure 9. Due to these

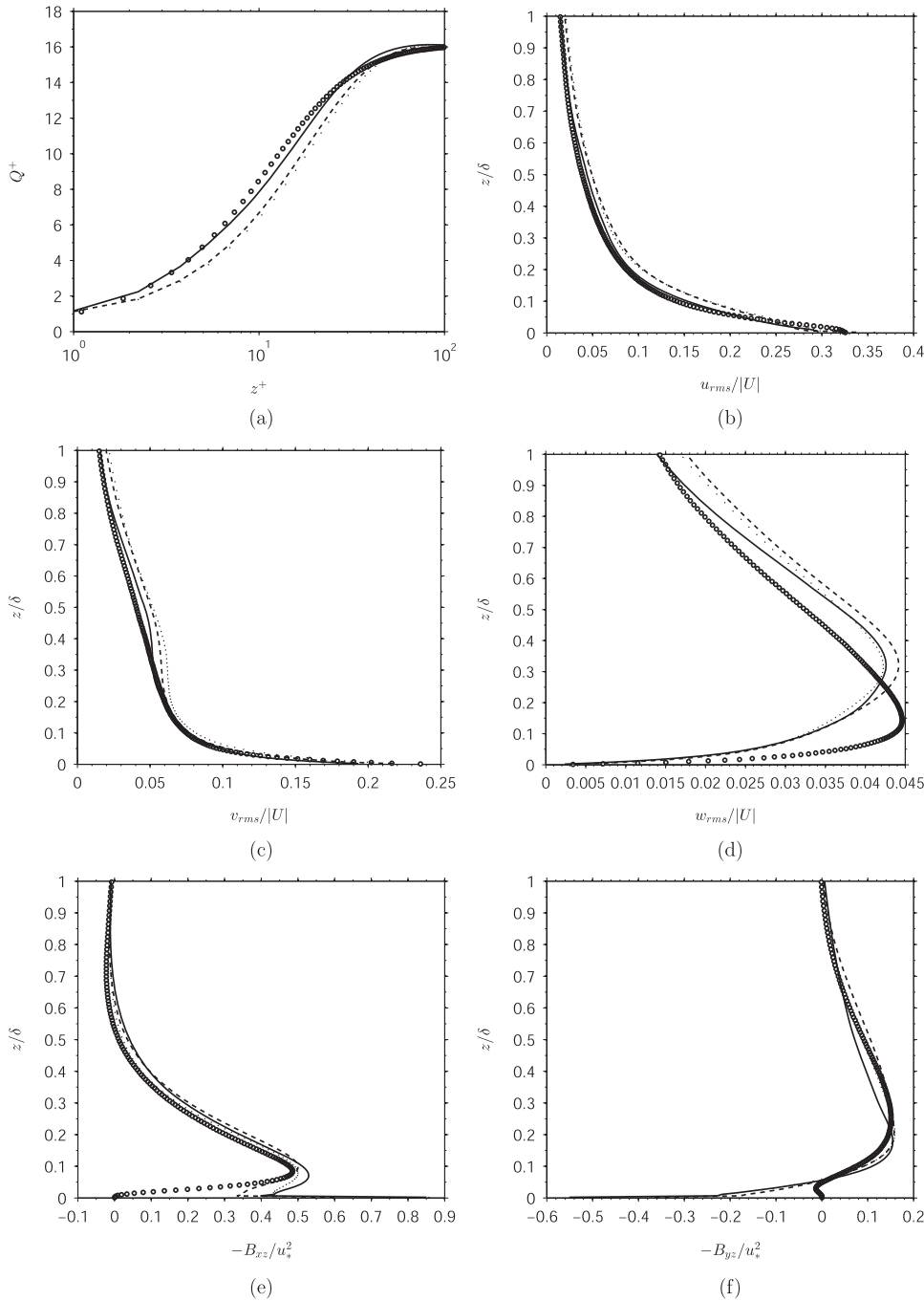


Figure 17: SM: (a) Q^+ , (b) $u_{rms}/|U|$, (c) $v_{rms}/|U|$, (d) $w_{rms}/|U|$, (e) $-B_{xz}/u_*^2$, (f) $-B_{yz}/u_*^2$. DNS (open circles); A1 grid (solid line), A2 grid (dashed line), and A3 grid (dotted line) results.

reasons, the SM cannot be seen as an appropriate model for rotating flows.

6 Conclusions

The performance of three LES models was studied here with respect to simulations of the turbulent neutrally stratified Ekman layer. In particular, we considered the SM (a standard LES model without dynamic model parameter calculation), the stabilized DSM (a standard dynamic LES model), and the LDM (a realizable dynamic LES model). The specific focus was on the question of whether the new LDM, which was recently suggested on the basis of stochastic turbulence theory [15, 16], would offer advantages in comparison to the well known SM and stabilized DSM. In continuation to a prior channel flow analysis of basic model features [16], the current paper presents the first application of the LDM to a relatively complex flow affected by rotation. The results obtained can be summarized in the following way.

The analysis of SM model features reveals that the SM does not represent an appropriate model for the flow considered. The mean velocity and turbulence intensities are poorly predicted. The near wall behavior of total stresses B_{xz} and B_{yz} is incorrectly described as a consequence of the damping function applied. It is of interest that this fact applies to both B_{xz} and B_{yz} , which means the usual concept of designing damping functions to correct the shear stress is not applicable to such a flow that is significantly affected by rotation. With respect to instantaneous velocities, it turns out that the SM is not capable of producing structures that reveal the same tilting as seen in DNS: the tilting provided by the SM is in the opposite direction. The fine scale structure of turbulence is poorly represented because areas of positive and negative fluctuations are merged to much larger regions than seen in DNS.

The analysis of the stabilized DSM model also reveals significant shortcomings. The method used to stabilize the original DSM is effective in the sense that it reduces the generation of computational instabilities, such that the stabilized DSM can be applied in simulations. However, this advantage causes some unphysical features of the stabilized DSM. In contrast to the behavior of all PDFs far away from the wall and corresponding LDM features, the stabilized DSM model implies that negative C_S values are more likely than positive C_S values. This is not a desired physical feature because it disagrees with the local equilibrium model. The stabilized DSM also suffers from the problem of a relatively long period of

negative correlations that generates computational instabilities. This fact indicates that the stabilized DSM incorporates a stable mechanism for generating negative dynamic model parameter values which generate computational instabilities. With respect to turbulence simulations it turns out that the stabilized DSM predicts mean fields comparably well as the LDM. However, the analysis of instantaneous velocity fields reveals two significant disadvantages. A first shortcoming of the stabilized DSM is that its behavior depends on the wall distance. Close to the wall, the stabilized DSM produces acceptable turbulence structures that agree, basically, with DNS. However, away from the wall the stabilized DSM suffers from exactly the same shortcomings as the SM (see the discussion in Section 5.2). A second shortcoming becomes obvious by looking at the effect of grid coarsening on instantaneous velocities. As shown in Section 5.3, the way of stabilizing the DSM corresponds to the introduction of face-average-induced-correlations. They may have positive effects by the promotion of LES-type motions. However, it is a random effect. For another flow or at another Reynolds number, the inclusion of such unphysical correlations may cause significant negative effects on turbulence predictions.

The analysis of LDM model features shows that the LDM is free from the disadvantages reported above regarding the use of the SM and stabilized DSM. The LDM is much more effective than the stabilized DSM with respect to the reduction of the range of negative C_S values. In contrast to both the original DSM and stabilized DSM, the LDM does not suffer from the problem of a relatively long period of negative correlations that may generate computational instabilities. The LDM produces a mean velocity and stresses that agree well with DNS data. It produces instantaneous velocity fields that show the same fine scale turbulence structures close and away from the wall as seen in DNS. The effect of grid variations correctly shows that a gradual grid coarsening leads to a gradual reduction of turbulent stresses.

Overall, the demonstrated shortcomings of the non-dynamic SM are not very surprising, but the following fact is surprising: the use of a dynamic LES method represents a mean for correctly simulating large-scale structures (means and stresses), but it does not ensure a correct simultaneous simulation of small scale structures. Our results indicate that the latter is only the case if the dynamic method is designed in consistency with a realizable stress model (as given for the LDM). This conclusion has relevant implications. It means that a dynamic LES method does not have predictive power in general (such that it can be used without evidence as an alternative to

DNS to simulate moderate Reynolds number flows). On the other hand, the results reported here support the view that the LDM has such predictive power because large and small scale structures can be correctly represented simultaneously.

Acknowledgments: The authors are very thankful to Prof. M. Stöllinger for interesting discussions and helpful suggestions for improvements. The authors are also thankful to the referees for their very helpful comments. Computational resources provided through the University of Wyoming are gratefully acknowledged.

Funding: This work was sponsored by the University of Wyoming School of Energy Resources via a graduate assistantship for E. Kazemi Froushani. The authors are very thankful for additional support from the National Renewable Energy Laboratory (NREL) monitored by Dr. Mike Robinson. The authors would like to acknowledge the support for this work through a gift from BP Alternative Energy North America Inc. to the UW Wind Energy Research Center. S. Heinz would like to acknowledge the partial support through NASA's NRA research opportunities in aeronautics program (Grant No. NNX12AJ71A) with Dr. P. Balakumar as the technical officer.

References

- [1] P. A. Durbin and B. A. Petterson, *Statistical theory and modeling for turbulent flows*, John Wiley and Sons, Chichester, New York, Weinheim, Brisbane, Singapore, Toronto, 2001.
- [2] S. Heinz, On Fokker-Planck equations for turbulent reacting flows. Part 1. Probability density function for Reynolds-averaged Navier–Stokes equations, *Flow Turbul. Combust.* **70** (2003), 115–152.
- [3] S. Heinz, On equations for turbulent reacting flows. Part 2. Filter density function for large eddy simulation, *Flow Turbul. Combust.* **70** (2003), 153–181.
- [4] S. Heinz, *Statistical mechanics of turbulent flows*, Springer, Berlin, Heidelberg, New York, 2003.
- [5] S. Heinz, Unified turbulence models for LES and RANS, FDF and PDF simulations, *Theor. Comput. Fluid Dyn.* **21** (2007), 99–118.
- [6] M. Lesieur, O. Métais, and P. Comte, *Large-eddy simulations of turbulence*, Cambridge University Press, Cambridge, UK, 2005.
- [7] S. B. Pope, *Turbulent flows*, Cambridge University Press, Cambridge, UK, 2000.
- [8] P. Sagaut, *Large eddy simulation for incompressible flows*, Springer, Berlin, Heidelberg, New York, 2002.
- [9] M. Germano, A dynamic subgrid-scale eddy viscosity model, *J. Fluid Mech.* **238** (1992), 325–336.
- [10] M. Germano, U. Piomelli, P. Moin and W. H. Cabot, A dynamic subgrid-scale eddy viscosity model, *Phys. Fluids A* **3** (1991), 1760–1765.
- [11] S. Ghosal, T. S. Lund, P. Moin and A. N. D. K. Akselvoll, A dynamic localization model for large-eddy simulation of turbulent flows, *J. Fluid Mech.* **286** (1995), 229–255.
- [12] D. K. Lilly, A proposed modification of the Germano subgrid-scale closure method, *Phys. Fluids A* **4** (1992), 633–635.
- [13] C. Meneveau, T. S. Lund and W. H. Cabot, A Lagrangian dynamic subgrid-scale model for turbulence, *J. Fluid Mech.* **319** (1996), 353–385.
- [14] H. Gopalan, S. Heinz and M. Stöllinger, A unified RANS-LES model: computational development, accuracy and cost, *J. Comput. Phys.* **249** (2013), 249–279.
- [15] S. Heinz, Realizability of dynamic subgrid-scale stress models via stochastic analysis, *Monte Carlo Method. Appl.* **14** (2008), 311–329.
- [16] S. Heinz and H. Gopalan, Realizable versus non-realizable dynamic sub-grid scale stress models, *Phys. Fluids* **24** (2012), 115105/1–23.
- [17] G. N. Coleman, Similarity statistics from a direct numerical simulation of the neutrally stratified planetary boundary layer, *J. Atmos. Sci.* **56** (1999), 891–900.
- [18] G. N. Coleman, J. H. Ferziger and P. R. Spalart, A numerical study of the Ekman layer, *J. Fluid Mech.* **213** (1990), 313–348.
- [19] S. Marlatt, S. Waggy and S. Biringen, Direct numerical simulation of the turbulent Ekman layer: turbulent energy budgets, *J. Thermophys. Heat Transfer* **24** (2010), 544–555.
- [20] W. Marlatt, *Direct numerical simulation of Ekman layer transition and turbulence*, PhD Thesis, University of Colorado, Boulder, 1994.
- [21] K. Miyashita, K. Iwamoto and H. Kawamura, Direct numerical simulation of the neutrally stratified turbulent Ekman boundary layer, *J. Earth Simul.* **6** (2006), 3–15.
- [22] K. Shingai and H. Kawamura, Direct numerical simulation of turbulent heat transfer in the stably stratified Ekman layer, *Therm. Sci. Eng.* **10** (2002), 25–33.
- [23] K. Shingai and H. Kawamura, A study of turbulent structure and large-scale motion in the Ekman layer through direct numerical simulations, *J. Turbul.* **5** (2004), 1–18.
- [24] J. R. Taylor and S. Sarkar, Direct and large eddy simulations of a bottom Ekman layer under an external stratification, *Int. J. Heat Fluid Flow* **29** (2008), 721–732.
- [25] S. Waggy, S. Marlatt, and S. Biringen, Direct numerical simulation of the turbulent EKMAN layer: instantaneous flow structures, *J. Thermophys. Heat Transfer* **25** (2011), 309–318.
- [26] D. K. Lilly, The representation of small-scale turbulence in numerical simulation of experiments, in: *Proceedings of the IBM Scientific Computing Symposium on Environmental Sciences*. H. H. Goldstine, ed., pp. 195–210, IBM, Yorktown Heights, NY, 1967.
- [27] E. D. Villiers, *The potential of large eddy simulation for the modelling of wall bounded flows*, PhD Thesis, Imperial College, London, 2006.
- [28] P. J. Mason, Large-eddy simulation of the convective atmospheric boundary layer, *J. Atmos. Sci.* **46** (1989), 1492–1516.
- [29] P. J. Mason and D. J. Thomson, Stochastic backscatter in large eddy simulation of boundary layers, *J. Fluid Mech.* **242** (1992), 51–78.

- [30] P. A. Durbin and C. G. Speziale, Realizability of second-moment closure via stochastic analysis, *J. Fluid Mech.* **280** (1994), 395–407.
- [31] S. B. Pope, On the relationship between stochastic Lagrangian models of turbulence and second-moment closures, *Phys. Fluids* **6** (1994), 973–985.
- [32] U. Schumann, Realizability of Reynolds stress turbulence models, *Phys. Fluids* **20** (1977), 721–725.
- [33] C. G. Speziale, R. Abid and P. A. Durbin, New results on the realizability of Reynolds stress turbulence closures, ICASE Report, 93–76 (1993), 1–47.
- [34] <http://murasun.me.noda.tus.ac.jp/turbulence/>.
- [35] E. Kazemi Froushani, Direct and large eddy simulation of the turbulent Ekman layer, PhD Thesis, University of Wyoming, Laramie, 2014.
- [36] Openfoam, the open source cfd tool box, user guide, see www.openfoam.org, tech. report, April 2014.
- [37] S. Heinz, *Mathematical modeling*, 1st ed. Springer-Verlag, Heidelberg, Dordrecht, London, New York, 2011.
- [38] P. Saha, S. Heinz, E. Kazemi Froushani and M. Stollinger, Turbulence structure characteristics of LES methods implied by stochastic turbulence models, in 52nd AIAA Aerospace Sciences Meeting and Exhibit, AIAA Paper 14–0592, National Harbor, MD, January 2014.
- [39] M. Bohnert and J. H. Ferziger, The dynamic subgrid scale model in large eddy simulation of the stratified Ekman layer, in: *Engineering Turbulence Modelling and Experiments 2*, W. Rodi and F. Martelli, eds, pp. 315–324, Elsevier, New York, 1993.